Ultrafine Mn_3O_4 nanowires synthesized by colloidal method as electrode materials for supercapacitors with a wide voltage range

Qisheng Fang[a], Mengxuan Sun[a], Xiaohe Ren[a], Baobao Cao[b], Wenzhong Shen[c], Zhijie Li[a,*], YongQing Fu[d,*]

[a] School of Physics, University of Electronic Science and Technology of China, Chengdu, 610054, P. R. China

[b] Key Laboratory of Advanced Technologies of Materials, Ministry of Education, Southwest Jiaotong University, Chengdu 610031, PR China

[c] State Key Laboratory of Coal Conversion, Institute of Coal Chemistry, Chinese Academy of Science, Taiyuan, 030001, P. R. China

[d] Faculty of Engineering and Environment, Northumbria University, Newcastle Upon Tyne, NE1 8ST, UK

Zhijie Li (**Corresponding Author**): ORCID: 0000-0001-9870-9939;

*E-mail: zhijieli@uestc.edu.cn; TEL: +86 02883202160

Yongqing Fu (**Corresponding Author**): ORCID: 0000-0001-9797-4036;

*E-mail: Richard.fu@northumbria.ac.uk; TEL: +44 (0)191 2274662

Abstract:

Manganese oxide is considered an ideal pseudo-capacitive electrode material for supercapacitors due to its low cost, environmental friendliness and large theoretical capacity. However, it is difficult to obtain manganese oxide electrodes with a high specific capacitance and a large voltage range. In this study, ultrafine Mn_3O_4 nanowires with an average diameter of 4.0 nm were synthesized using a colloidal method. They have a large specific surface area of 175.1 $m^2\ g^{-1}$, and can provide numerous active sites to enhance their specific capacitances. They also show a large pore volume of 0.7960 $cm^3\ g^{-1}$, which can provide essential channels for ion transport during charging and discharging processes. The supercapacitor electrode made of these ultrafine Mn_3O_4 nanowires exhibits a predominant surface capacitive behavior during charge/discharge processes, and achieves a large specific capacitance of 433.1 F g^{-1} at a current density of 0.5 A g^{-1} with a very wide voltage range from -0.5 to 1.1 V in 1 M Na_2SO_4 electrolyte. An asymmetric supercapacitor (ASC) was assembled using a cathode electrode made of these ultrafine Mn_3O_4 nanowires and an active carbon (AC) anode electrode, and a high energy density of 26.68 Wh kg^{-1} at a power density of 442 W kg^{-1} was achieved. The ASC showed a good cycling stability, and its capacitance value was still maintained at 75.8% after 64000 charge/discharge cycles.

Key words: Mn_3O_4, Ultrafine nanowires, Supercapacitor, Pseudo-capacitance, Electrochemical property

1 Introduction

Along with the rapid development and application of electronic devices, there is a critical demand for high storage devices with high power and energy density. Due to its excellent cycle stability, fast charging speed, high power density, high rate capability, environmental friendliness and safe operation, supercapacitor (SC) is regarded as one of the key energy storage devices [1-4]. So far, various types of electrode materials for supercapacitor devices have been studied, such as carbon materials, metal oxides and sulfides, as well as conducting polymers. Supercapacitor electrode materials are divided into three types according to their different energy storage mechanisms: battery type [5], electric double-layer capacitance (EDLC) type [6] and pseudo-capacitance type [7]. The battery type materials, such as Co_3O_4 [8], $Ni(OH)_2$ [9] and CuO [10], can achieve charging and discharging by moderating transfer of valence electrons by phase transition and diffusion control, but their poor reversibility and slow dynamics lead to their poor long-term stability [11, 12]. The energy storage principle for the EDLC materials (mainly the carbon materials) is based on the accumulation of static charges between the electrode materials and the electrolyte interface. Although their electrochemical performance is relatively stable, their capacitance values are relatively low. Pseudo-capacitor electrodes are based on rapid and reversible Faraday redox reactions between the active substance and electrolyte ions on their surfaces for energy storage, which makes these pseudo-capacitors having a potentially high specific capacitance and an excellent cycle stability.

Up to now, many types of pseudo-capacitive electrode materials have been

discovered, such as ruthenium oxides [13-15] and manganese oxides [16-19]. Ruthenium oxides are regarded as ideal pseudo-capacitor electrode materials due to their high specific capacitance of 760 F g^{-1}, good electrical conductivity and cycle stability [15]. However, they are expensive, toxic and often difficult to prepare [20]. Manganese oxides are one of the excellent substitutes for the ruthenium oxides because of their low cost, easy preparation methods and non-toxicity [18]. They have various crystal structures and high theoretical capacitances [19], and thus currently attract extensive attention.

As a transition metal oxide, manganese oxides have various valences, and thus have different electrochemical properties. Common manganese oxides include MnO, MnO_2, Mn_2O_3 and Mn_3O_4. Among these, Mn_3O_4 has excellent electrochemical properties because it has two valence states, e.g., +2 and +3, which can generate reversible Faraday redox reactions [21]. In general, Mn_3O_4 SC electrode materials are controlled by the capacitive behavior based on the Faraday redox reactions on their surfaces [22]. Therefore, a large specific surface area of the electrode is beneficial for increasing the number of active sites, thereby improving the efficiency of Faraday redox reactions and achieving a higher capacitance. The uniquely nanostructured Mn_3O_4 can provide a large specific surface area and numerous channels for ion transport in the charging and discharging processes, thus improving the specific capacitance.

Various nanostructures of Mn_3O_4 have been applied as the SC electrode materials, including nanoparticles [18, 23, 24], nanorods [25, 26], nanowires [28] and nanosheet [29]. Many methods have been applied to prepare Mn_3O_4 nanostructures for the SC

electrode materials, and these include hydrothermal method [18, 29, 30], sol-gel method [22, 31], pulsed laser deposition (PLD) [19], and chemical precipitation method [24]. For example, Song *et al*. reported Mn_3O_4 nanoparticles which prepared using a chemical precipitation method, and these Mn_3O_4 nanoparticles were used as the electrode for the SC, which showed a specific capacitance of 112 F g^{-1} at a current density of 1 A g^{-1} [24]. Anikumar *et al*. prepared Mn_3O_4 nanorods using a hydrothermal method and then applied them as the electrode for SC, which showed a specific capacitance of 144 F g^{-1} at a scan rate of 5 mV s^{-1} [26]. Mn_3O_4 nanowires were prepared using an annealing process after a chemical reaction in an alkaline condition, and they were used as the electrode for SC, which showed a capacitance of 277 F g^{-1} at a scan rate of 1 mV s^{-1} [27]. Mn_3O_4 nanosheets prepared using a chemical deposition method were applied as the electrode of SC, which achieved a specific capacitance of 127 F g^{-1} at a scan rate of 10 mV s^{-1} [28]. All these reported values of specific capacitances are quite low. Besides, according to the calculation formula of energy density: $E=C\times V^2/(2\times 3.6)$ [32, 33], the operating voltage ranges plays a pivotal role in acquiring high energy densities of SC. However, the working voltage range of SC electrodes made of manganese oxides reported in the literature are usually less than 1 V [24, 26-28] Therefore, it is critical to obtain new type of manganese oxide nanostructures, which can be used as the SC electrodes with a high specific capacitance and a large voltage range.

In this study, ultrafine Mn_3O_4 nanowires were prepared using a colloidal method assisted by cetyltrimethyl ammonium bromide (CTAB) and sodium borohydride

($NaBH_4$) at room temperature. The SC electrode made of these nanowires showed a high specific capacitance, up to 433.1 F g^{-1}, and a very wide voltage range of -0.5V~1.1V. An asymmetric supercapacitor (ASC) was fabricated by using the Mn_3O_4 as the cathode electrode and active carbon (AC) as the anode electrode, and exhibited good electrochemical properties.

2 Experimental section

2.1 Preparation of electrode materials

The reagents used in the study were all in their analytical grades and not further treated, and these include sodium borohydride ($NaBH_4$), manganese chloride tetrahydrate ($MnCl_2·4H_2O$), hexadecyl trimethyl ammonium bromide (CTAB), nickel foam, carbon black, polytetrafluoroethylene (PTFE) and sodium sulfate (Na_2SO_4).

Firstly, $MnCl_2·4H_2O$ (0.7916 g) and CTAB (1.8 g) were added into 100 mL of deionized water and stirred for 10 minutes. Then 5 ml of sodium borohydride solution (1 mol L^{-1}) was added inside the above solution, and a large number of bubbles were generated. The solution was continually stirred until these bubbles disappeared and a colloid was formed. Then, the colloid was left for one hour at room temperature in air and the brown precipitates were collected. The precipitates were separated from the solution by centrifugation, and washed with deionized water and alcohol for three times, and dried at 60 °C for 12 hours. Then, the precipitates were annealed in a muffle furnace at 500 °C for two hours in air to obtain the Mn_3O_4 nanowires.

2.2 Characterization of materials

An X-ray diffractometer (XRD, Rigaku D/max-2400, α=0.15406 nm, 40 kV, Cu Kα radiation) was used to characterize the crystalline structures of the Mn_3O_4 nanowires. Morphology, chemical composition and crystallinity of the ultrafine Mn_3O_4 nanowires were characterized using a high-resolution transmission electron microscope (HRTEM, JEOL JEM-2200F) attached with an energy-dispersive X-ray spectroscope (EDS). Chemical states of elements for the ultrafine Mn_3O_4 nanowires were analyzed using an X-ray photoelectron spectrometer (XPS, Kratos Axis-Ultra DLD) with an Al Kα radiation source. Brunauer–Emmett–Teller (BET) method were applied to measure the specific surface area and pore structure using a Micromeritics ASAP2460 instrument, and the Barrett-Joyner-Harunda (BJH) method were used calculate the pore size distribution and pore volume.

2.3 Electrochemical measurements

Electrochemical performance of ultrafine Mn_3O_4 nanowires based supercapacitor electrode was evaluated using a CHI660E electrochemical workstation (CHI660E, Shanghai Chenhua Device Company, China). Testing methods include cyclic voltammetry (CV), galvanostatic charge–discharge (GCD) and electrochemical impedance spectroscopy (EIS), all characterized at room temperature. The EIS was performed with an open circuit voltage and an alternate voltage amplitude of 5.0 mV in the frequency range of 0.01~100 kHz.

To prepare the electrode, ultrafine Mn_3O_4 nanowires as the active material, AC and PTFE were added into ethanol according to the mass ratio of 8:1:1 to make a slurry. The slurry was coated onto the nickel foam (1.0×1.0 cm^2) and dried. The coated nickel

foam was pressed at 10 MPa for 1 min, and these ultrafine Mn_3O_4 nanowires electrode were used as the working electrode. To evaluate these electrodes' performance, they were tested in a three-electrode system. A platinum plate was used as the counter electrode, and a saturated calomel electrode was used as the reference electrode. The electrolyte was a 1 M Na_2SO_4 aqueous solution.

An asymmetric supercapacitor (ASC) device was further made using the Mn_3O_4 nanowires as the cathode electrode, an active carbon (AC) as the anode electrode, and 1 M Na_2SO_4 aqueous solution as the electrolyte. The AC anode electrode was prepared in the same way as the ultrafine Mn_3O_4 nanowires electrode. According to the charge balance theory, the mass ratio of the ultrafine Mn_3O_4 nanowires and active carbon is about 1:3 based on the following equation (1) [34]:

$$\frac{m_+}{m-} = \frac{C_- \times \Delta V_-}{C_+ \times \Delta V_+} \quad (1)$$

A battery test instrument system (CT3001A, LAND Electronic Co. Ltd) was used to characterize the cycling performance of the Mn_3O_4//AC ASC device.

3 Results and discussion

3.1 Material characterization

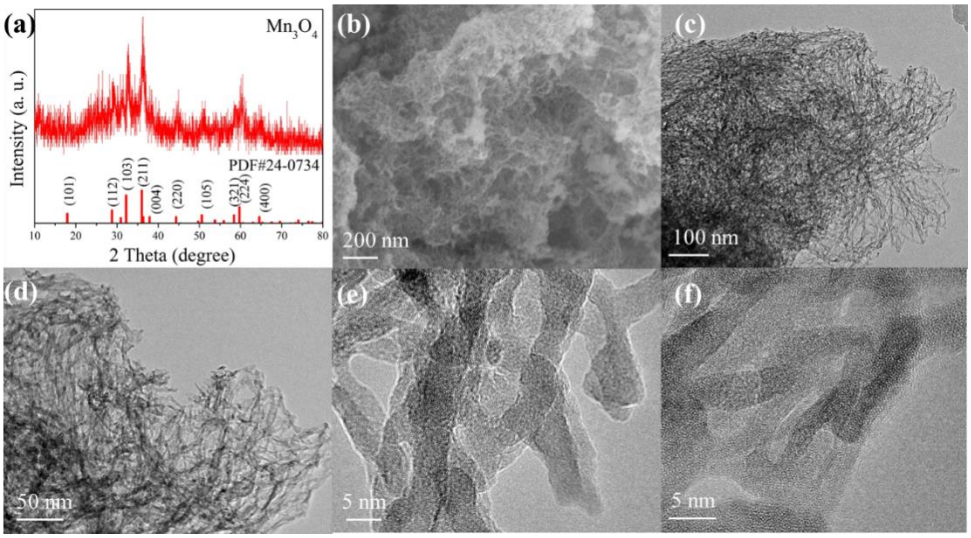

Fig. 1 (a) XRD spectrum, (b) SEM, (c, d) TEM and (e, f) HRTEM images of Mn_3O_4 sample.

Fig. 1a shows the XRD spectrum of Mn_3O_4 nanowires samples. The main peaks are corresponding to (103), (211) and (224) planes of the hausmannite Mn_3O_4 (JCPDS card no. 24-0734), and these peaks are quite broadened, which indicates that these Mn_3O_4 sample have a relatively poor crystallinity, or very small crystals. Fig. 1b shows the SEM image of Mn_3O_4 sample. It can be seen that the Mn_3O_4 sample is composed of ultrafine nanowires. Figs. 1c and 1d shows TEM images of Mn_3O_4 sample, and the Mn_3O_4 has a network structure composed of ultrafine nanowires. In addition, from the HRTEM images shown in Figs. 1e and 1f, these ultrafine nanowires do not show clearly defined crystalline structures, which is consistent with the XRD analysis result. Based on these HRTEM images, the average diameter of these nanowires is only about 4.0 nm.

According to equation (2) [35], $NaBH_4$ undergoes a spontaneous hydrolysis to release hydrogen gas in the solution of $MnCl_2 \cdot 4H_2O$, which produces a large number of bubbles in the solution due to the usage of CTAB. Based on equation (3), the $NaBO_2$

is further hydrolyzed, which produces OH^-, thus resulting in the formation of alkaline conditions in the solution. Meanwhile, according to equation (4), Mn^{2+} ions are transformed into $Mn(OH)_2$ nanoclusters. According to equation (5), after the hydrogen gas bubbles disappear, oxygen molecules in the air are re-dissolved into the solution and quickly react with $Mn(OH)_2$ nanoclusters to form Mn_3O_4 nanostructures.

$$NaBH_4 + 2H_2O \rightarrow NaBO_2 + 4H_2\uparrow \quad (2)$$

$$BO_2^- + 2H_2O \rightarrow B(OH)_3 + OH^- \quad (3)$$

$$2Mn^{2+} + 4OH^- \rightarrow 2Mn(OH)_2 \quad (4)$$

$$2Mn(OH)_2 + 2O_2 \rightarrow Mn_3O_4\downarrow + 6H_2O \quad (5)$$

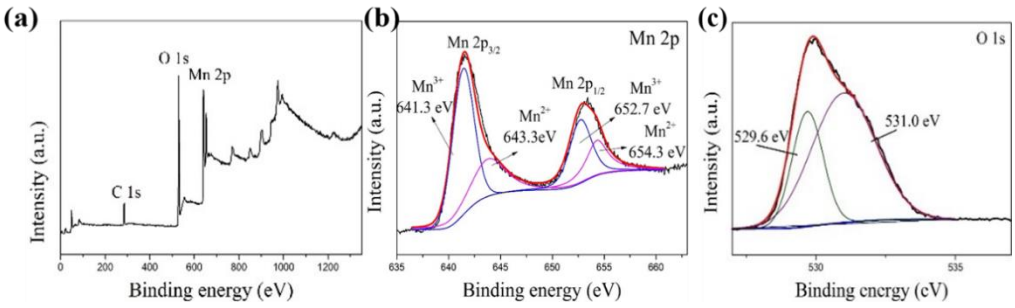

Fig .2(a) XPS survey spectrum of the Mn_3O_4 nanowires, and high-resolution XPS spectra of (b) Mn 2p and (c) O 1s.

Chemical states and elemental composition of Mn_3O_4 nanowire electrodes were further analyzed using XPS. The XPS survey spectrum of Mn_3O_4 nanowires is shown in Fig. 2a, and the peaks of Mn and O elements can be clearly observed. As shown in Fig. 2b, the high resolution XPS spectrum of Mn 2p can be divided into two peaks of Mn $2p_{1/2}$ and Mn $2p_{3/2}$ peaks. The Mn $2p_{1/2}$ peak can be deconvoluted into two peaks located at 654.3 and 652.7 eV, which are assigned to Mn^{2+} $2p_{1/2}$ and Mn^{3+} $2p_{1/2}$. The Mn $2p_{3/2}$ peak can also be deconvolved into two peaks and they are located at 643.3 and

641.3 eV, which can be assigned to Mn^{2+} $2p_{3/2}$ and Mn^{3+} $2p_{3/2}$ [36]. According to the area under each peak, the ratio of Mn^{2+} and Mn^{3+} on the surface can be calculated as about 1:2. Based on both the XPS and XRD analysis results, we can confirm that the Mn_3O_4 was successfully prepared [37]. Fig. 2c shows the high-resolution spectrum of O 1s, in which the peaks at 529.6 and 531.0 eV refer to the O atoms in the Mn–O–Mn lattices and the hydroxyl groups on the surface of Mn_3O_4 nanowires, respectively [38]. Based on the area under each peak, the ratio between the O atoms in lattices and the hydroxyl group on the surface was calculated to be 9:20, indicating that there are lots of hydroxyl groups on the surfaces of ultrafine Mn_3O_4 nanowires due to their large specific surface areas.

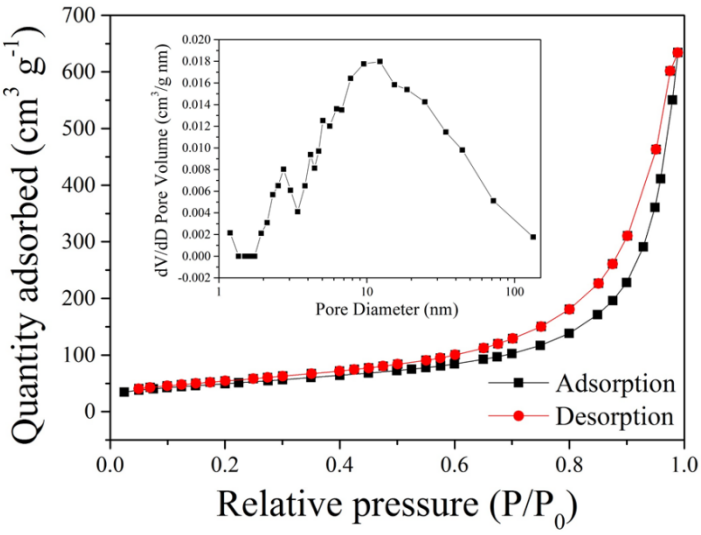

Fig. 3 N_2 adsorption/desorption isotherm of Mn_3O_4 ultrafine nanowires (inset shows the pore size distributions).

The BET surface areas and nanostructures of the Mn_3O_4 nanowires were further investigated based on the N_2 adsorption-desorption isotherm. As shown in Fig. 3, the obtained curve shows a type-IV isotherm characteristic [39], indicating that mesoporous structures are formed in these ultrafine Mn_3O_4 nanowires. The pore sizes

are ranged from 1.5 nm to 100 nm but mainly centered at 12.3 nm with a large pore volume of 0.7960 $cm^3 g^{-1}$ (see the inset in Fig. 3). The two peaks in the inset in Fig. 3 indicate that the mesoporous structure is composed of two parts, e.g., the former one centered at 2.7 nm is provided by the internal structure of Mn_3O_4 nanowires, and the latter one centered at 12.3 nm is resulted from the accumulation of Mn_3O_4 nanowires. Because of the ultrafine size and large porosity, the Mn_3O_4 nanowires show a very large BET surface area of 175.1 $m^2 g^{-1}$. Therefore, the ultrafine nanowire morphology, large surface area and large porosity of the Mn_3O_4 nanowires can provide numerous active sites on the surfaces of ultrafine Mn_3O_4 nanowires for the Faradaic redox reactions and lots of pathways for the diffusion of electrolyte ions, all of which are beneficial for achieving a large specific capacitance.

3.3 Electrochemical properties of Mn_3O_4 nanowires based electrodes

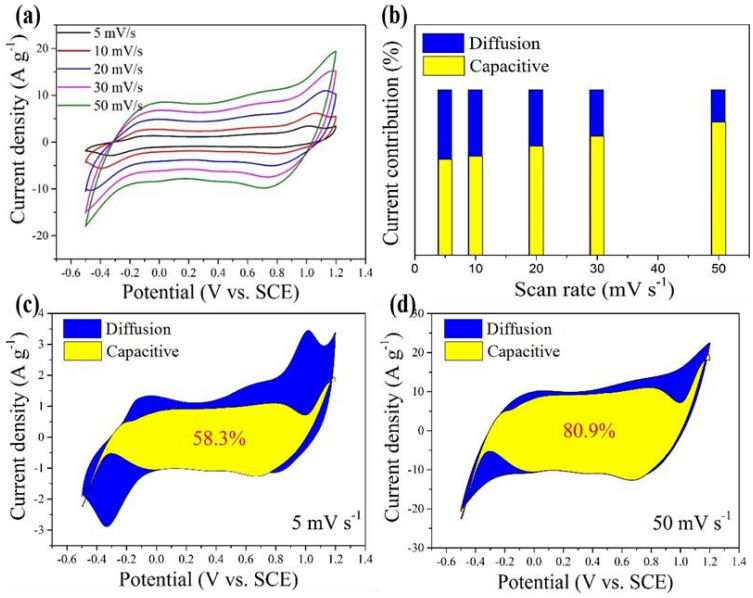

Fig. 4 (a) CV curves of Mn_3O_4 nanowire electrodes at different scan rates, (b) the contribution of diffusion and capacitive at different scan rate, (c, d) the contribution of capacitive in the CV curve at 5 mV s^{-1} and 50 mV s^{-1}

To examine electrochemical properties of Mn_3O_4 nanowire electrodes, the CV curves with scan rates of 5 mV s^{-1}, 10 mV s^{-1}, 20 mV s^{-1}, 30 mV s^{-1}, 50 mV s^{-1} were measured, and the obtained results are displayed in Fig. 4a. It shows that Mn_3O_4 nanowire electrodes can work in a very wide voltage range from -0.5 to 1.1 V. This value is the largest range of working voltage reported for the manganese oxide based SC electrodes so far, which we have summarized in Table 1. At all the scan rates, the CV curves show almost a quadrilateral shape, and there are small redox peaks in these CV curves. The peak positions of the positive and negative scans show minor shifts, indicating that the Mn_3O_4 nanowire electrodes have both pseudo-capacitance and battery-type characteristics in the charging and discharging processes.

Using the equation (6) [40], the surface capacitive contribution and diffusion-controlled contribution in charging/discharging process of Mn_3O_4 nanowire electrodes can be calculated:

$$i(V) = k_1 v + k_2 v^{\frac{1}{2}} \quad (6)$$

where i is the current value (mA), V is the fixed potential (V), k_1 and k_2 are the constants, which can be obtained from the fitting plots of $i/v^{\frac{1}{2}}$ versus $k_2 v^{\frac{1}{2}}$, $k_1 v$ is the contribution of the surface capacitive behavior, $k_2 v^{\frac{1}{2}}$ is the contribution of diffusion-controlled behavior. As shown in Fig. 4b, the proportion of capacitive-type behavior is increased with the increase of scan rate. As shown in the Figs. 4c and 4d, the capacitive-type behavior occupies about 58.3% of the total capacitance at 5 mV s^{-1}. When the scan rate is increased to 50 mV s^{-1}, the capacitive-type behavior ratio is then increased to 80.9%. Most of the capacitive-type behaviors are found at a range between -0.3V~1V.

Therefore, the capacitive-type behavior is predominant in the charging/discharging process of Mn_3O_4 nanowire electrodes.

The energy storage of Mn_3O_4 electrode materials in an aqueous electrolyte is following the proton-electron mechanism [41]. Because there are lots of hydroxyl groups on the surface of the Mn_3O_4 ultrafine nanowires, the electrochemical reaction can be described using the following equation (7) [42].

$$MnO_x(OH)_y+\delta H^+ +\delta e^- \leftrightarrow MnO_{x-\delta}(OH)_{y+\delta} \quad (7)$$

In this equation, $MnO_x(OH)_y$ is the manganese oxide species at a higher oxidation state, and the $MnO_{x-\delta}(OH)_{y+\delta}$ is the one at a lower oxidation state, respectively. In addition, Ref [43] reported that the cation in the electrolyte will affect the reaction process of charge and discharge, as listed in the following equation (8):

$$MnO_x(OH)_y+\delta Na^+ +\delta e^- \leftrightarrow Na_\delta MnO_{x-\delta}(OH)_y \quad (8)$$

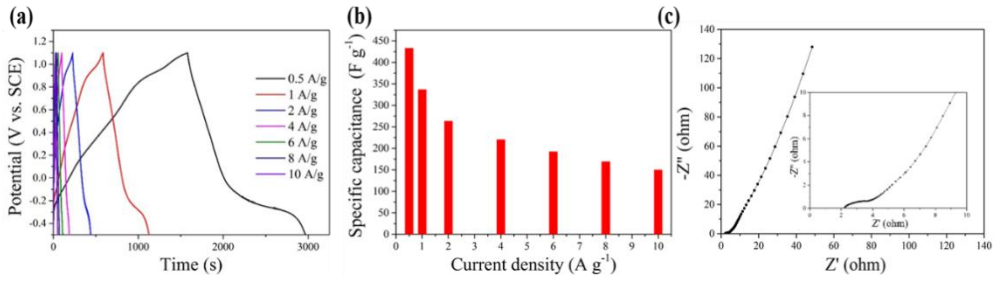

Fig. 5 (a) GCD curves at different current densities, (b) specific capacitance at different current densities and (c) Nyquist plots of the Mn_3O_4 nanowire electrodes.

Fig. 5a shows the GCD curves at different specific currents within a voltage range of -0.5~1.1 V. As shown in the GCD curves, with the increase of current density, the redox platform becomes decreased significantly, and the proportion of the capacitance provided by diffusion-controlled behavior is gradually decreased. Based on the GCD curves, the specific capacitance values of Mn_3O_4 nanowire electrodes can be calculated

according to equation (9) [44]:

$$Cs=\frac{I\times t}{m\times \Delta V} \quad (9)$$

where I is the discharge current (mA), t is the discharge time (s), m is the mass of Mn_3O_4 (mg) on electrode and ΔV is the voltage range (V) in the GCD curves. The obtained specific capacitance results are shown in Fig. 5b, and they are 433.1, 336.9, 263.8, 220.5, 192.4, 169.0 and 150.0 F g^{-1} at 0.5, 1, 2, 4, 6, 8 and 10 A g^{-1}, respectively. It can maintain 44.53% of capacitance from 1 A g^{-1} to 10 A g^{-1}. Table 1 lists the capacitance values and voltage range of manganese oxide electrodes reported in literature. Compared with the reported values for manganese oxide electrodes, the Mn_3O_4 nanowire electrodes in this study shows the largest capacitance value and the widest voltage range. Even compared with the electrodes made of the modified Mn_3O_4 by graphene, the Mn_3O_4 ultrafine nanowire electrode still exhibits a better electrochemical performance. [45-48].

Table 1. Summary of electrochemical properties of other manganese oxide electrodes in literature.

Materials	**Preparation method**	**Electrolyte**	**Potential Window (V)**	**Capacitance (F g^{-1})**
Graphene@Mn_3O_4 [45]	Chemical vapor deposition	1 M Na_2SO_4	-0.2~0.8	208.3 at 0.5 A g^{-1}
rGO/Mn_3O_4 nanoparticles [46]	Co-precipitation	1 M Na_2SO_4	0~0.8	248.1 at 5 mV s^{-1}
Mn_3O_4/rGO nanowalls [47]	Chemical precipitation	0.5 M KOH	0~1	310 at 1 A g^{-1}
rGO/ Mn_3O_4 nanoflakes [48]	Co-precipitation	1 M Na_2SO_4	-0.2~0.8	351 at 0.5 A g^{-1}
MnO_2/Mn_3O_4 nanowires [49]	Hydrothermal	1 M Na_2SO_4	0~1	181 at 2 A g^{-1}
Nd_2O_3/Mn_3O_4 nanoparticles [50]	Hydrothermal	3 M KOH	-0.2-0.5	205.3 at 5 mV s^{-1}
Mn_3O_4TB/NHPC [51]	Ultrasonic assembly	1 M Na_2SO_4	0~0.8	366.0 at 0.5 A g^{-1}
Mn_3O_4 microcubes [30]	Hydrothermal	1 M Na_2SO_4	-0.2~0.8	176.0 at 0.3 A g^{-1}
Mn_3O_4 nanowalls [52]	Electrochemical deposition	1 M Na_2SO_4	0~1	300.7 at 5 mV s^{-1}
MnO_2@NiO nanosheets [53]	Hydrothermal	1 M KOH	-0.2~0.45	374.6 at 0.25 A g^{-1}
Mn_2O_3@MnO_2 nanofibers [16]	Hydrothermal	1 M Na_2SO_4	0~1	225.0 at 0.2 A g^{-1}
Mn_2O_3@Carbon [54]	Hydrothermal	0.5 M Na_2SO_4	-0.65~0.35	235.9 at 0.05 A g^{-1}

Mn_3O_4 nanowires (This work)	Colloidal method	1 M Na_2SO_4	-0.5~1.1	433.1 at 0.5 A g^{-1}

Note: rGO: reduced graphene oxide; TB: tetragonal bipyramid; NHPC: nitrogen doped and hierarchically porous carbon.

EIS tests were further conducted in order to study the interfacial electrochemical kinetics of Mn_3O_4 nanowire electrodes in the Na_2SO_4 electrolyte. The open-circuit voltage was set at 5 mV and the frequency range was 10^{-2} ~10^5 Hz. The obtained Nyquist plots are shown in Fig. 5c. In the high frequency range, a small semicircular diameter can be found, which is corresponding to the charge transfer resistance (R_{ct}), caused by the Faraday reaction between the electrode material and the electrolyte ions [55, 56]. The intercept at the x-axis is the internal resistance (R_s) [57, 58], which includes the inherent resistance of the electrolyte and electrode material, and the contact resistance between the electrode material and collector. The Mn_3O_4 nanowire electrodes show small resistance values: e.g., R_s (2.16 Ω) and R_{ct} (2.31 Ω), suggesting their excellence in the ion transport efficiency. Ion diffusion in the dielectrics affects the slope of the low frequency linear part of the Nyquist plots, which corresponds to the Warburg impedance behavior (R_w) [59]. The Nyquist plots of an ideal battery-type material should show a large semicircle in the low frequency region and the angle between the straight line of the high frequency region and the x-axis should be about 45°. While the pseudo-capacitance material should have a small semicircle in the low frequency region and the straight line of the high frequency region is about 90° to the x-axis [60]. It can be seen from the Nyquist plots of the Mn_3O_4 nanowire electrodes in Fig. 5c that slope in the low frequency linear part is approximately 67°. The low frequency semicircle is not as large as those of the standard battery type materials, which means that both the surface control and diffusion control act together for the

Mn_3O_4 nanowire electrode.

The stability of the ultrafine Mn_3O_4 nanowires electrode was tested in the three-electrode system at the current density of 6 A g^{-1}, and the result is showed in Fig. S1, the capacitance decreased rapidly in the first 200 cycles, but then remained relatively stable, which can maintain 72.6% after 4000 cycles. And the SEM images and XRD spectra of the Mn_3O_4 electrode are not obviously changed before and after cycling as shown in Fig. S2, indicating that the structure of the Mn_3O_4 is stable in the charge-discharge processed.

Furthermore, the Mn_3O_4 electrode was tested in three electrode system at the voltage range of 0~1.2 V. In the CV curves and the GCD curves (see Figs. S3a and 3b), there are no obvious REDOX peaks or REDOX platform within the voltage range of 0~1.2 V. The calculated capacitance values at different current densities are shown in Fig. S3c. The capacitance value of Mn_3O_4 electrode is 202.8 F g^{-1} at the current density of 1 A g^{-1}, and it can maintain 63.2% when the current density is increased to 10 A g^{-1}.

3.4 Electrochemical performance of Mn_3O_4//AC ASC

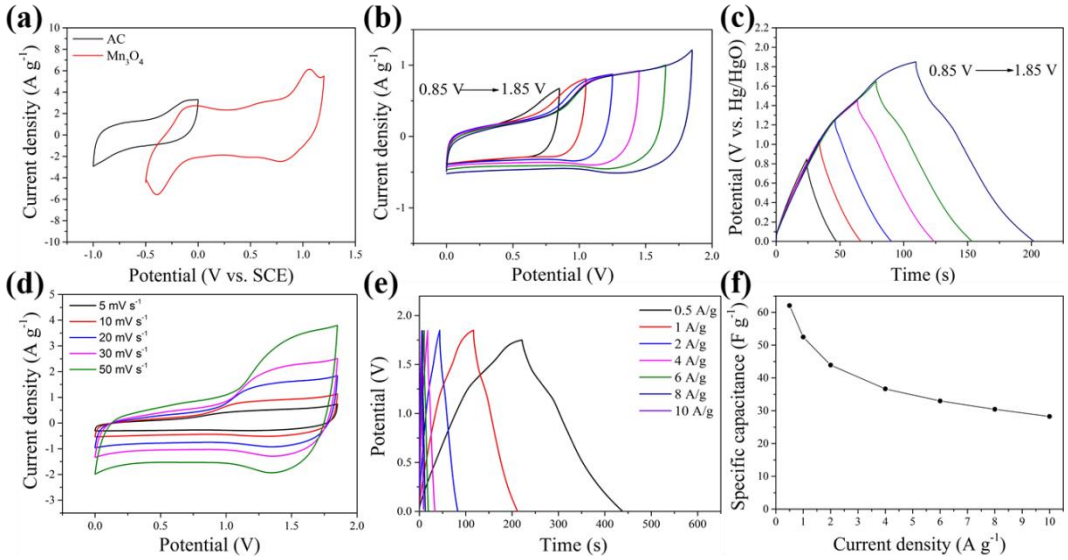

Fig. 6 (a) CV curves of ultrafine Mn_3O_4 nanowires and AC at 10 mV s^{-1}, (b) CV curves and (c) GCD curves of Mn_3O_4//AC ASC at various voltage range, (d) CV curves of Mn_3O_4//AC ASC at various scan rates, (e) GCD curves and (f) corresponding specific capacitance values of the Mn_3O_4//AC ASC at various current densities.

In order to evaluate the application of Mn_3O_4 nanowire electrodes for electrochemical energy storage, a Mn_3O_4//AC ASC were assembled, in which ultrafine Mn_3O_4 nanowires was used as the cathode electrode and AC as the anode electrode. The CV curves of ultrafine Mn_3O_4 nanowire and AC electrodes at a scan rate of 10 mV s^{-1} are shown in Fig. 6a. The stable operating voltage of this ASC device can be as large as 1.85 V. Figs. 6b and 6c are the CV curves and GCD curves of Mn_3O_4//AC ASC under different voltage ranges, respectively. It can be seen that the performance of the Mn_3O_4//AC ASC is very stable in the 1.85 V voltage range. Fig. 6d shows the CV curves at different scan rates, and there are no significant changes in CV curves at different scan rates. They are all stable with a fixed shape, indicating that the ASC has a good

pseudo-capacitance characteristic. According to the GCD curves shown in Fig. 6e, at different current densities, the specific capacity of Mn_3O_4//AC ASC can be calculated according to the following equation (10) [61]:

$$C_d = \frac{I \times t}{M \times \Delta V} \tag{10}$$

where I (A), t (s), M (g) and ΔV (V) are corresponding to the applied constant discharge current, the discharge time, the total mass of Mn_3O_4 and AC, and the voltage range of Mn_3O_4//AC ASC, respectively. When the current density is 1 A g^{-1}, the capacitances of the Mn_3O_4//AC is 52.5 F g^{-1}.

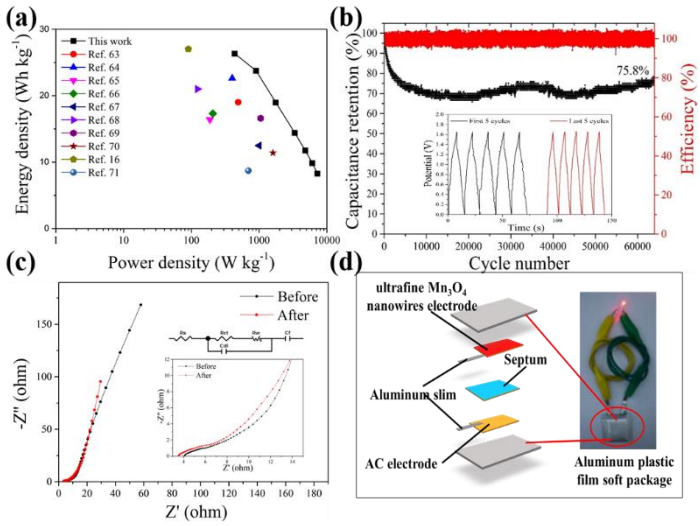

Fig. 7 (a) Ragone plots; (b) cycling performance (inset photograph is GCD curves of first and last 5 cycles); (c) Nyquist plots and (d) structure diagram of pouch cell (inset a lighted LED bulb with the pouch cell.)

Based on the previously calculated specific capacitance (C_d) of Mn_3O_4//AC ASC, the energy density (E, Wh kg^{-1}) and power density (P, W kg^{-1}) of Mn_3O_4//AC ASC can be calculated using the following equations (11) and (12) [34, 62]:

$$E = \frac{C_d \times \Delta V^2}{2 \times 3.6} \tag{11}$$

$$P = \frac{E \times 3600}{\Delta t} \quad (12)$$

As shown in Fig. 7a, the energy density of Mn_3O_4//AC ASC can reach 26.7 Wh kg^{-1} at a power density of 442 W kg^{-1}, which is higher than many reported ASC devices assembled with manganese oxide and different negative electrodes. These include Mn_3O_4-fCNT//ZnO-CNT (19 Wh kg^{-1} at 490 W kg^{-1}) [63], Mn_3O_4 (22.6 Wh kg^{-1} at 400 W kg^{-1}) [64], Mn_3O_4//Bi_2O_3 (16.4Wh kg^{-1} at 187.5W kg^{-1}) [65], Mn_3O_4//Mn_3O_4/NC (17.3 Wh kg^{-1} at 207.3 W kg^{-1}) [66], MnS@ Mn_3O_4/C//AC (12.5 Wh kg^{-1} at 1000 W kg^{-1}) [67], MnO2/CNT//AC (21 Wh kg^{-1} at 123 W kg^{-1}) [68], MnO_x@rGO//rGO (16.6 Wh kg^{-1} at 1052 W kg^{-1}) [69], MnO_2@BL//NBL ASC (11.4 Wh kg^{-1} at 1600 W kg^{-1}) [70], Mn_2O_3@MnO_2//AC (27 Wh kg^{-1} at 90 W kg^{-1}) [16] and MnO_2@Fe_2O_3 (8.7 Wh kg^{-1} at 694 W kg^{-1}) [71].

The cyclic stability of $MnCo_2O_4$@Ni_3S_4//AC ASC was tested at a current density of 8 A g^{-1}, and the results are shown in Fig. 7b. The capacitance of the Mn_3O_4//AC ASC still maintains 75.8% of its initial value after 64000 cycles, and the Coulomb efficiency has been kept at 99.8% in the whole process, indicating its excellent cyclic stability.

It should be noted that a small amount of Mn_3O_4 materials fell away from the working electrode in the initial 1000 cycles, which caused the decreased of the capacitance of Mn_3O_4//AC ASC. We have tried different ways to solve this problem, but it is hard to avoid it completely. Preventing the loss of the Mn_3O_4 active materials from the electrode to improve the stability of ASC is the goal of our further research. As shown in the inset in Fig.7b, the GCD curves have no significant changes before and after the cycling process. The EIS results of the Mn_3O_4//AC ASC before and after cycling test

were also obtained, and the obtained Nyquist plots of the Mn_3O_4//AC ASC are shown in Fig. 7c. Smaller values of Rs (3.4 Ω) and Rct (7.0 Ω) were obtained after 64,000 charge/discharge cycles. Compared with the Rs and Rct of 4.0 Ω and 4.7 Ω before cycling, the Rs value has been reduced, probably because in the process of circulation, there are good contact between the active materials and electrolyte. However, the Rct values are obviously increased, which shows that the charge transfer efficiency has been reduced. As the value of Rct is still maintained a low value, this proves that the Mn_3O_4//AC ASC maintains a good electrochemical performance after a long-term charging and discharging process.

The Mn_3O_4//AC ASC was assembled into a pouch cell as shown in Fig. 7d. An aluminum slim film was used as the packaging material, and a filter paper as for septum containing 1 M Na_2SO_4 solution was used as the diaphragm. Mn_3O_4 electrode and AC electrode were connected with aluminum strips, respectively. The LED lamp has been successfully lit as shown in the inset of Fig. 7d.

In this work, the CV curves of AC electrode and the ultrafine Mn_3O_4 nanowire electrode are not perfectly matched, and there is overlapped between -0.5~0 V, although this will not have a great impact on the performance of the supercapacitor. In the future work, by exploring other anode materials to match with the ultrafine Mn_3O_4 nanowire electrode, the asymmetric supercapacitors with better electrochemical performance can be obtained.

4 Conclusions

Mn_3O_4 ultrafine nanowires were successfully synthesized using a colloidal method, and they have large specific surface areas, large pore volumes and abundant active sites. The Mn_3O_4 ultrafine nanowire based electrodes exhibited a large specific capacitance. It showed a capacitive-type behavior and a battery-type behavior in charging/discharging processes, and capacitive-type behavior was found to be dominant. The assembled Mn_3O_4//AC device achieved a high energy density of 26.7 Wh kg^{-1} at a power density of 442 W kg^{-1}. After 64000 cycles, it can still maintain 75.8% of the initially capacitance value. Therefore, due to the good electrochemical properties of the ultrafine Mn_3O_4 nanowires, it can be used as an active material for supercapacitors. By preventing the loss of the Mn_3O_4 nanowires from the electrode and exploring other anode materials to match with the Mn_3O_4 nanowire electrode, it is hopefully to achieve asymmetric supercapacitors with excellent electrochemical performance.

Acknowledgements

This work is supported by International Exchange Grant (IEC/NSFC/201078) through Royal Society and the National Natural Science Foundation of China (NSFC).

References

[1] H. Wang, W. Cai, L. He, M. Zhu, Y. Wang, Anchoring ternary NiCoMn-S ultrathin nanosheets on porous $ZnCo_2O_4$ nanowires to form core-shell composites for high-performance asymmetric supercapacitor, J. Alloy. Compd., 870 (2021) 159347.

[2] Z. Liang, R. Zhao, T. Qiu, R. Zou, Q. Xu, Metal-organic framework-derived materials for electrochemical energy applications, EnergyChem., 1 (2019) 100001.

[3] M. Du, Q. Li, Y. Zhao, C.-S. Liu, H. Pang, A review of electrochemical energy storage behaviors based on pristine metal–organic frameworks and their composites, Coord. Chem. Rev., 416 (2020) 213341.

[4] S. Zhou, P. Huang, T. Xiong, F. Yang, H. Yang, Y. Huang, D. Li, J. Deng, M.J.T. Balogun, Sub-Thick Electrodes with Enhanced Transport Kinetics via in Situ Epitaxial Heterogeneous Interfaces for High Areal-Capacity Lithium Ion Batteries, Small, 17 (2021) 2100778.

[5] Y. Zhu, P. Lu, F. Li, Y. Ding, Y. Chen, Metal-rich porous copper cobalt phosphide nanoplates as a high-rate and stable battery-type cathode material for battery–supercapacitor hybrid devices, ACS Appl. Energ. Mater., 4 (2021) 3962-3974.

[6] M.C. Fite, T. Imae, Capacitance enhancement of nitrogen-doped graphene oxide/magnetite with polyaniline or carbon dots under external magnetic field: Supported by theoretical estimation, J. Colloid. Interf. Sci., 594 (2021) 228-244.

[7] S.G. Kandalkar, H.-M. Lee, S.H. Seo, K. Lee, C.-K. Kim, Preparation and characterization of the electrodeposited Ni-Co oxide thin films for electrochemical capacitors, Korean J. Chem. Eng., 28 (2011) 1464-1467.

[8] Y. Zhang, J. Cao, Z. Yuan, L. Zhao, L. Wang, W. Han, Assembling Co_3O_4 nanoparticles into MXene with Enhanced electrochemical performance for advanced asymmetric supercapacitors, J. Colloid. Interf. Sci., 599 (2021) 109-118.

[9] L. He, Y. Wang, Y. Guo, G. Li, X. Zhang, W. Cai, Core-shell NiSe/$Ni(OH)_2$ with

NiSe nanorods and $Ni(OH)_2$ nanosheets as battery-type electrode for hybrid supercapacitors, Nanotechnology, 32 (2021) 345706.

[10] M. Zhai, A. Li, J. Hu, CuO nanorods grown vertically on graphene nanosheets as a battery-type material for high-performance supercapacitor electrodes, RSC Adv., 10 (2020) 36554-36561.

[11] J. Cao, Y. Hu, Y. Zhu, H. Cao, M. Fan, C. Huang, K. Shu, M. He, H.C. Chen, Synthesis of mesoporous nickel-cobalt-manganese sulfides as electroactive materials for hybrid supercapacitors, Chem. Eng. J., 405 (2021) 126928.

[12] M. Du, Q. Li, G. Zhang, F. Wang, H. Pang, Metal–Organic Framework−Based Sulfur−Loaded Materials, Energy Environ. Mater., 0 (2021) 1-16.

[13] B. Djurfors, J.N. Broughton, M.J. Brett, D.G. Ivey, Electrochemical oxidation of Mn/MnO films: formation of an electrochemical capacitor, Acta Mater., 53 (2005) 957-965.

[14] S. Asim, M.S. Javed, J. Khan, M. Khalid, S.S.A. Shah, M. Idrees, M. Imran, M. Usman, S. Hussain, I. Ahmad, T.S. AlGarni, Energy storage performance of binder-free ruthenium-oxide nano-needles based free-standing electrode in neutral pH electrolytes, Electrochim. Acta, 378 (2021) 138139.

[15] S.-H. Ryu, S.-G. Hwang, S.-R. Yun, K.-K. Cho, K.-W. Kim, K.-S. Ryu, Synthesis and electrochemical characterization of silica-manganese oxide with a core-shell structure and various oxidation states, B. Korean Chem. Soc., 32 (2011) 2683-2688.

[16] W. Lu, Y. Li, M. Yang, X. Jiang, Y. Zhang, Y. Xing, Construction of hierarchical Mn_2O_3@MnO_2 core-shell nanofibers for enhanced performance supercapacitor

electrodes, ACS Appl. Energ. Mater., 3 (2020) 8190-8197.

[17] S. Nagamuthu, K.-S. Ryu, MOF-derived microstructural interconnected network porous Mn_2O_3/C as negative electrode material for asymmetric supercapacitor device, Crystengcomm, 21 (2019) 1442-1451.

[18] Y. Wu, S. Liu, H. Wang, X. Wang, X. Zhang, G. Jin, A novel solvothermal synthesis of Mn_3O_4/graphene composites for supercapacitors, Electrochim. Acta, 90 (2013) 210-218.

[19] D. Yang, Pulsed laser deposition of manganese oxide thin films for supercapacitor applications, J. Power Sources, 196 (2011) 8843-8849.

[20] M.S. Yadav, Synthesis and characterization of Mn_2O_3-Mn_3O_4 nanoparticles and activated charcoal based nanocomposite for supercapacitor electrode application, J. Energy Storage, 27 (2020) 101079.

[21] V.C. Bose, V. Biju, Mixed valence nanostructured Mn_3O_4 for supercapacitor applications, B. Mater. Sci., 38 (2015) 865-873.

[22] M. Mohamed Ismail, S. Hemaanandhan, D. Mani, M. Arivanandhan, G. Anbalagan, R. Jayavel, Facile preparation of Mn_3O_4/rGO hybrid nanocomposite by sol-gel in situ reduction method with enhanced energy storage performance for supercapacitor applications, J. Sol-Gel. Sci. Techn., 93 (2020) 703-713.

[23] E.R. Kavitha, S. Meiyazhagan, S. Yugeswaran, P. Balraju, K. Suresh, Electrochemical prospects and potential of hausmannite Mn_3O_4 nanoparticles synthesized through microplasma discharge for supercapacitor applications, Int. J. Energ. Res., 45 (2021) 7038-7056.

[24] Y.Z. Song, L.C. Zhu, Z.Z. Zhang, J.J. Ding, A facile synthesis of azoviolet@Mn_3O_4 nanoparticles for supercapacitor, Russ. J. Phys. Chem. A, 91 (2017) 1987-1993.

[25] H. Park, M.Y. Kang, Effects of voluntary/involuntary retirement on their own and spouses' depressive symptoms, Compr. Psychiat., 66 (2016) 1-8.

[26] K.M. Anilkumar, M. Manoj, B. Jinisha, V.S. Pradeep, S. Jayalekshmi, Mn_3O_4/reduced graphene oxide nanocomposite electrodes with tailored morphology for high power supercapacitor applications, Electrochim. Acta, 236 (2017) 424-433.

[27] H.-M. Luo, F.-B. Zhang, P. Yang, Preparation and electrochemical properties of CPAC/Mn_3O_4 nanocomposite electrode, J. Mater. Sci-Mater. El., 24 (2013) 601-606.

[28] D.P. Dubal, R. Holze, All-solid-state flexible thin film supercapacitor based on Mn_3O_4 stacked nanosheets with gel electrolyte, Energy, 51 (2013) 407-412.

[29] S.K. Godlaveeti, S. Jangiti, A.R. Somala, H. Maseed, R.R. Nagireddy, Different Phase and Morphology Effect of Manganese Oxide on Electrochemical Performance for Supercapacitor Application, J. Clust. Sci., 32 (2021) 703-710.

[30] Z. Liu, L. Zhang, G. Xu, L. Zhang, D. Jia, C. Zhang, Mn_3O_4 hollow microcubes and solid nanospheres derived from a metal formate framework for electrochemical capacitor applications, RSC Adv., 7 (2017) 11129-11134.

[31] C.C. Chen, C.-Y. Yang, C.-K. Lin, Improved pseudo-capacitive performance of manganese oxide films synthesized by the facile sol-gel method with iron acetate addition, Ceram. Int., 39 (2013) 7831-7838.

[32] W. Luo, G. Zhang, Y. Cui, Y. Sun, Q. Qin, J. Zhang, W. Zheng, One-step extended strategy for the ionic liquid-assisted synthesis of Ni_3S_4-MoS_2 heterojunction electrodes

for supercapacitors, J. Mater. Chem. A, 5 (2017) 11278-11285.

[33] K.-B. Wang, Q. Xun, Q. Zhang, Recent progress in metal-organic frameworks as active materials for supercapacitors, EnergyChem., 2 (2020) 100025.

[34] H. Li, Z. Li, Z. Wu, M. Sun, S. Han, C. Cai, W. Shen, Y. Fu, Nanocomposites of cobalt sulfide embedded carbon nanotubes with enhanced supercapacitor performance, J. Electrochem. Soc., 166 (2019) A1031-A1037.

[35] Y. Zhou, Y. Wu, P. Zhang, J. Chen, B. Qu, J.T. Li, Co_3O_4@(Fe-Doped)$Co(OH)_2$ microfibers: facile synthesis, oriented-assembly, formation mechanism, and high electrocatalytic activity, ACS Appl. Mater. Inter., 9 (2017) 30880-30890.

[36] N. Li, Y. Tian, J. Zhao, J. Zhang, J. Zhang, W. Zuo, Y. Ding, Efficient removal of chromium from water by Mn_3O_4@ZnO/Mn_3O_4 composite under simulated sunlight irradiation: Synergy of photocatalytic reduction and adsorption, Appl. Catal. B-Environ., 214 (2017) 126-136.

[37] Z.-Y. Tian, P. Mountapmbeme Kouotou, N. Bahlawane, P.H. Tchoua Ngamou, Synthesis of the catalytically active Mn_3O_4 spinel and its thermal properties, J. Phys. Chem. C, 117 (2013) 6218-6224.

[38] H. Li, Z. Li, M. Sun, Z. Wu, W. Shen, Y.Q. Fu, Zinc cobalt sulfide nanoparticles as high performance electrode material for asymmetric supercapacitor, Electrochim. Acta, 319 (2019) 716-726.

[39] G. Bharath, N. Arora, A. Hai, F. Banat, D. Savariraj, H. Taher, R.V. Mangalaraja, Synthesis of hierarchical Mn_3O_4 nanowires on reduced graphene oxide nanoarchitecture as effective pseudocapacitive electrodes for capacitive desalination

application, Electrochim. Acta, 337 (2020).

[40] N. Zhao, H. Fan, M. Zhang, J. Ma, C. Wang, A.K. Yadav, H. Li, X. Jiang, X. Cao, Beyond intercalation-based supercapacitors: The electrochemical oxidation from Mn_3O_4 to $Li_4Mn_5O_{12}$ in Li_2SO_4 electrolyte, Nano Energy, 71 (2020) 135668.

[41] G. An, P. Yu, M. Xiao, Z. Liu, Z. Miao, K. Ding, L. Mao, Low-temperature synthesis of Mn_3O_4 nanoparticles loaded on multi-walled carbon nanotubes and their application in electrochemical capacitors, Nanotechnology, 19 (2008) 275709.

[42] C.-C. Hu, T.-W. Tsou, The optimization of specific capacitance of amorphous manganese oxide for electrochemical supercapacitors using experimental strategies, J. Power Sources, 115 (2003) 179-186.

[43] M. Wu, G.A. Snook, G.Z. Chen, D.J. Fray, Redox deposition of manganese oxide on graphite for supercapacitors, Electrochem. Commun., 6 (2004) 499-504.

[44] M.X. Sun, Z.J. Li, H. Li, Z.L. Wu, W.Z. Shen, Y.Q. Fu, Mesoporous Zr-doped CeO_2 nanostructures as superior supercapacitor electrode with significantly enhanced specific capacity and excellent cycling stability, Electrochim. Acta, 331 (2020) 10.

[45] T. Wang, Q. Le, X. Guo, M. Huang, X. Liu, F. Dong, J. Zhang, Y.X. Zhang, preparation of porous graphene@Mn_3O_4 and its application in the oxygen reduction reaction and supercapacitor, ACS Sustain. Chem. Eng., 7 (2019) 831-837.

[46] B.S. Singu, K.R. Yoon, Exfoliated graphene-manganese oxide nanocomposite electrode materials for supercapacitor, J. Alloy. Compd., 770 (2019) 1189-1199.

[47] P.K. Jha, V. Kashyap, K. Gupta, V. Kumar, A.K. Debnath, D. Roy, S. Rana, S. Kurungot, N. Ballav, In-situ generated Mn_3O_4-reduced graphene oxide nanocomposite

for oxygen reduction reaction and isolated reduced graphene oxide for supercapacitor applications, Carbon, 154 (2019) 285-291.

[48] Z. Huang, S. Li, Z. Li, J. Li, G. Zhang, L. Cao, H. Liu, Mn_3O_4 nanoflakes/rGO composites with moderate pore size and (O=) C-O-Mn bond for enhanced supercapacitor performance, J. Alloy. Compd., 830 (2020) 154637.

[49] J. Jia, X. Lian, M. Wu, F. Zheng, Y. Gao, H. Niu, Self-assembly of alpha-MnO_2/Mn_3O_4 hierarchical structure on carbon cloth for aymmetric supercapacitors, J. Mater. Sci., 56 (2021) 3246-3255.

[50] K.T. Kubra, R. Sharif, B. Patil, A. Javaid, S. Shahzadi, A. Salman, S. Siddique, G. Ali, Hydrothermal synthesis of neodymium oxide nanoparticles and its nanocomposites with manganese oxide as electrode materials for supercapacitor application, J. Alloy. Compd., 815 (2020) 152104.

[51] Y. Cheng, B. Li, Z. Wei, Y. Wang, D. Wei, D. Jia, Y. Feng, Y. Zhou, Mn_3O_4 tetragonal bipyramid laden nitrogen doped and hierarchically porous carbon composite as positive electrode for high-performance asymmetric supercapacitor, J. Power Sources, 451 (2020) 227775.

[52] K.S. Kumar, J. Cherusseri, J. Thomas, Two-dimensional Mn_3O_4 nanowalls grown on carbon fibers as electrodes for flexible supercapacitors, ACS Omega, 4 (2019) 4472-4480.

[53] X. Zhao, X. Liu, F. Li, M. Huang, MnO_2@NiO nanosheets@nanowires hierarchical structures with enhanced supercapacitive properties, J. Mater. Sci., 55 (2020) 2482-2491.

[54] Y. Fu, F. Liu, H. Wang, Spindle Mn_2O_3/carbon hybrid with homogeneous structure as advanced electrodes for supercapacitors, J. Nanopart. Res., 22 (2020) 22-32.

[55] Q. Zhang, H. Liu, Y. Xu, L. Wang, 3D nanoflower-like zinc hydroxyl carbonates for high performance asymmetric supercapacitors, J. Solid State Chem., 267 (2018) 76-84.

[56] Y. Huang, H. Yang, T. Xiong, D. Adekoya, W. Qiu, Z. Wang, S. Zhang, M.S. Balogun, Adsorption energy engineering of nickel oxide hybrid nanosheets for high areal capacity flexible lithium-ion batteries, Energy Storage Mater., 25 (2020) 41-51.

[57] X. Wang, L. Tian, X. Long, M. Yang, X. Song, W. Xie, D. Liu, Y. Fu, J. Li, Y. Li, D. He, Cracked bark-inspired ternary metallic sulfide ($NiCoMnS_4$) nanostructure on carbon cloth for high-performance aqueous asymmetric supercapacitors, Sci. China-Mater., 64 (2021) 1632-1641.

[58] T. Xiong, H. Su, F. Yang, Q. Tan, P.B.S. Appadurai, A.A. Afuwape, K. Guo, Y. Huang, Z. Wang, M.S. Balogun, Harmonizing self-supportive VN/MoS_2 pseudocapacitance core-shell electrodes for boosting the areal capacity of lithium storage, Mater. Today Energy, 17 (2020) 100461.

[59] M. Sun, Z. Li, Q. Fang, S. Han, C. Cai, H. Li, W. Shen, X. Liu, Y. Fu, Room-temperature synthesized porous $Cu(OH)_2$/Cu_7S_4 hybrid nanowires as a high-performance electrode material for asymmetric supercapacitors, J. Mater. Chem. A, 8 (2020) 724-734.

[60] J. Xie, P. Yang, Y. Wang, T. Qi, Y. Lei, C.M. Li, Puzzles and confusions in supercapacitor and battery: Theory and solutions, J. Power Sources, 401 (2018) 213-

223.

[61] H. Li, Z. Li, Z. Wu, M. Sun, S. Han, C. Cai, W. Shen, X. Liu, Y. Fu, Enhanced electrochemical performance of $CuCo_2S_4$/carbon nanotubes composite as electrode material for supercapacitors, J. Colloid. Interf. Sci., 549 (2019) 105-113.

[62] P. Suktha, P. Chiochan, A. Krittayavathananon, S. Sarawutanukul, S. Sethuraman, M. Sawangphruk, In situ mass change and gas analysis of 3D manganese oxide/graphene aerogel for supercapacitors, RSC Adv., 9 (2019) 28569-28575.

[63] R. Ranjithkumar, S.E. Arasi, N. Nallamuthu, P. Devendran, P. Lakshmanan, A. Arivarasan, M.K. Kumar, Investigation and fabrication of asymmetrical supercapacitor using nanostructured Mn_3O_4 immobilized carbon nanotube composite, Superlattice. Microst., 138 (2020) 106380.

[64] X. Shi, S. Zhang, X. Chen, P.K. Chu, T. Tang, E. Mijowska, Formation of ultra-small Mn_3O_4 nanoparticles trapped in nanochannels of hollow carbon spheres by nanoconfinement with excellent supercapacitor performance, Int. J. Hydrogen Energ., 44 (2019) 13675-13683.

[65] Z. Li, W. Wei, Y. Wang, A. Gu, L. Wang, Q. Zhou, Trimanganese tetraoxide nanoframeworks: Morphology-controlled synthesis and application in asymmetric supercapacitors, J. Alloy. Compd., 793 (2019) 446-453.

[66] G. Wang, Z. Ma, Y. Fan, G. Shao, L. Kong, W. Gao, Preparation of size-selective Mn_3O_4 hexagonal nanoplates with superior electrochemical properties for pseudocapacitors, Phys. Chem. Chem. Phys., 17 (2015) 23017-23025.

[67] K. Krishnasamy, K.K. Purushothaman, Preparation and characterisation of MnS@

Mn_3O_4/C nanoflakes for hybrid supercapacitor applications, Mater. Technol., (2020) 1-8.

[68] V. Khomenko, E. Raymundo-Piñero, F. Béguin, Optimisation of an asymmetric manganese oxide/activated carbon capacitor working at 2V in aqueous medium, J. Power Sources, 153 (2006) 183-190.

[69] S.-Y. Hsu, S.-C. Lin, J.-A. Wang, C.-C. Hu, C.-C.M. Ma, D.-H. Tsai, Aerosol-based synthesis of silsesquioxane-graphene oxide and graphene-manganese oxide nanocomposites for high-performance asymmetric supercapacitors, Electrochim. Acta, 296 (2019) 427-437.

[70] J. Yu, M. Li, X. Wang, Z. Yang, promising high-performance supercapacitor electrode materials from MnO_2 nanosheets@bamboo leaf carbon, ACS Omega, 5 (2020) 16299-16306.

[71] G.S. Gund, D.P. Dubal, N.R. Chodankar, J.Y. Cho, P. Gomez-Romero, C. Park, C.D. Lokhande, Low-cost flexible supercapacitors with high-energy density based on nanostructured MnO_2 and Fe_2O_3 thin films directly fabricated onto stainless steel, Sci Rep-UK, 5 (2015) 13.